

Spontaneous Quantum Turbulence in a Newborn Bose-Einstein Condensate via the Kibble-Zurek Mechanism

Seong-Ho Shinn^{①,*}, Matteo Massaro^{②,†}, Mithun Thudiyangal^{③,4} and Adolfo del Campo^{②,5}

¹*Department of Physics and Materials Science, University of Luxembourg, L-1511 Luxembourg, Luxembourg*

²*Department of Physics and Materials Science, University of Luxembourg, L-1511 Luxembourg, Luxembourg*

³*Center for Quantum Technologies and Complex Systems (CQTCS),
Christ University, Bengaluru, Karnataka 560029, India*

⁴*Department of Physics and Electronics, Christ University, Bengaluru, Karnataka 560029, India*

⁵*Donostia International Physics Center, E-20018 San Sebastián, Spain*

The Kibble-Zurek mechanism (KZM) predicts the spontaneous formation of topological defects in a continuous phase transition driven at a finite rate. We propose the generation of spontaneous quantum turbulence (SQT) via the KZM during Bose-Einstein condensation induced by a thermal quench. Using numerical simulations of the stochastic projected Gross-Pitaevskii equation in two spatial dimensions, we describe the formation of a newborn Bose-Einstein condensate proliferated by quantum vortices. We establish the nonequilibrium universality of SQT through the Kibble-Zurek and Kolmogorov scaling of the incompressible kinetic energy.

Understanding turbulence is one of the long-standing unsolved problems in physics, with broad applications in biology, medicine, industry, and weather prediction [1, 2]. Feynman pioneered the idea of Quantum Turbulence (QT) as an analog in superfluids proliferated by a tangle of vortices [3]. With the development of technology to create, manipulate, and probe quantum fluids, the study of quantum turbulence emerged as a new research field at the frontiers of nonequilibrium physics of complex systems, arising in superfluid helium, Bose-Einstein condensates, polaritonic condensates, and neutron stars [4–10], with applications ranging from atomtronics to astrophysics.

The turbulent regime in quantum fluids describes the complex, chaotic dynamics of interacting quantized vortices, which are topological defects. This definition is loose, and as we shall see, different criteria for its diagnosis have been put forward, including the scaling of the energy spectrum on the wavenumber, velocity autocorrelation functions, circulation statistics, etc. The situation is reminiscent of the use of various inequivalent definitions of quantum chaos, emphasizing complementary features brought out by a diversity of diagnostic tools (spectral statistics, semiclassical orbits, out-of-time order correlators, etc.) [11].

QT was discovered in low-temperature physics studies of superfluid Helium. However, the remarkable experimental progress in the mid-90s offered a new highly controllable and tunable platform for its exploration: Bose-Einstein Condensates (BECs) of ultracold atomic gases [12] and the closely related quantum fluids of light [13]. The experimental measurement of quantized vortices in BEC was crucial in probing their superfluid character. A BEC is characterized by a macroscopic wavefunction that acts as a complex-valued order parameter and can be conveniently written in a polar decomposition $\Psi(\mathbf{r}) = \sqrt{\rho(\mathbf{r})} e^{i\theta(\mathbf{r})}$ [14]. A defining feature of a superfluid is that the circulation $\Gamma[C] = \oint_C \mathbf{v} \cdot d\ell$ (that

is, the contour integral of the velocity around a given contour C) is quantized as a result of the single-valued character of the macroscopic wavefunction and the relation between the superfluid velocity \mathbf{v} (equivalently, the vorticity $\boldsymbol{\omega} = \nabla \times \mathbf{v}$) and the condensate phase, $\mathbf{v}(\mathbf{r}) = \hbar \nabla \theta(\mathbf{r})/m$. QT differs from its classical counterpart in that quantum vortices are true topological defects and thus more stable than eddies, having conserved and quantized circulation [8, 15].

The phenomenology of turbulence varies significantly with the spatial dimension. In three spatial dimensions (3D), turbulence is characterized by a cascade of energy from large to small scales, with eddies breaking into ever-decreasing whirlpools. By contrast, two-dimensional (2D) turbulence is governed by the presence of an additional invariant of motion known as the enstrophy, and gives rise to an inverse energy cascade, with energy flowing from small to large scales. In the quantum case, the spatial dimensionality of the superfluid can be varied by tuning the anisotropy of the external confinement in BEC experiments. Notably, in 2D QT, enstrophy may not be conserved due to vortex-antivortex annihilation, and a direct energy cascade can therefore appear, as observed in numerical simulations [16, 17] and BECs experiments [18]. In contrast, its conservation leads to the clustering of vortices in bigger patches, a behavior predicted by Onsager and experimentally reported in BECs [19, 20] and exciton-polariton superfluids [21].

Several protocols are used to induce QT in a superfluid sample. They generally rely on continuous pumping of energy. A predominant approach involves sweeping a repulsive potential [22, 23]. This procedure is often too violent, complicating the study of QT, as a result of the generation of a variety of excitations. As an alternative, one may wonder whether QT can emerge spontaneously, as topological defects emerge across a continuous phase transition. We refer to the QT that arises through finite-time spontaneous symmetry breaking as

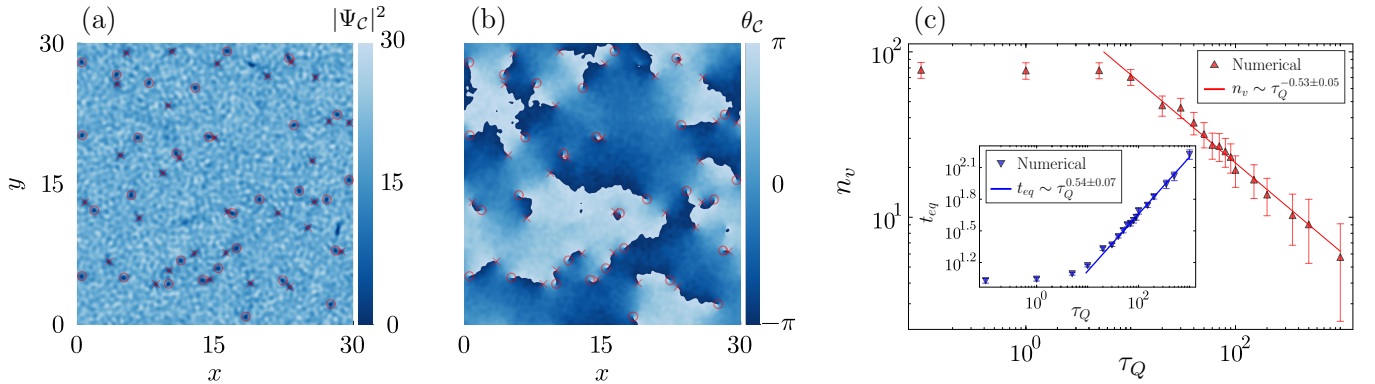


Figure 1. Typical condensate density and phase profiles at equilibration time, together with the vortex-number scaling. Panel (a) shows the condensate density $|\Psi_C(\mathbf{r}, t_{eq})|^2$ at equilibration time t_{eq} following a quench of duration $\tau_Q = 10$, while panel (b) displays the corresponding phase of Ψ_C . Vortices with topological charge $w = +1$ are marked by red crosses and those with $w = -1$ by circles; no vortices with $|w| > 1$ were observed. The main plot in panel (c) shows the vortex count n_v at t_{eq} versus quench time τ_Q , demonstrating the Kibble-Zurek power-law scaling for $10 \leq \tau_Q \leq 1000$. The inset plots t_{eq} against τ_Q , where t_{eq} is the equilibration time measured from the crossing of the critical point. Data are averaged over $\mathcal{R} = 1000$ realizations, with error bars indicating one standard deviation.

spontaneous quantum turbulence (SQT). In this context, the Kibble-Zurek mechanism (KZM) constitutes a powerful paradigm for describing universal critical dynamics [24–28]. It does so by exploiting equilibrium properties such as the divergence of the correlation length $\xi = \xi_0/|\varepsilon|^\nu$ and the relaxation time $\tau = \tau_0/|\varepsilon|^{z\nu}$ in the neighborhood of the critical point [28]. Here, ν and z are the correlation-length and dynamic critical exponents, $\varepsilon = (\lambda - \lambda_c)/\lambda_c$ with λ the control parameter (e.g., temperature) and λ_c its critical value, while ξ_0 and τ_0 are nonuniversal constants with dimensions of length and time, respectively. For a linearized quench $\varepsilon = t/\tau_Q$, the KZM introduces the universal scaling of the nonequilibrium correlation length $\hat{\xi}$ with the quench time τ_Q , i.e., $\hat{\xi} = \xi_0(\tau_Q/\tau_0)^{\nu/(1+z\nu)}$. For point-like defects, such as solitons in a cigar-shaped BEC [29, 30], and vortices in a pancake BEC [31, 32], the KZM further predicts the formation of vortices at a density ρ_v that scales universally with the quench time as $\rho_v \propto 1/\hat{\xi}^2 = (1/\xi_0^2)(\tau_0/\tau_Q)^{2\nu/(1+z\nu)}$. In addition, it dictates that the response of the system is delayed by the freeze-out time scale $\hat{t} = (\tau_0\tau_Q^{z\nu})^{1/(1+z\nu)}$. In scenarios characterized by symmetry breaking that lead to vortex formation, the KZM has been widely tested in theoretical studies [33–39], with several experiments also supporting its role in superfluid formation and the BEC transition [31, 40–42].

In this Letter, we establish and describe SQT in a newborn BEC prepared by a thermal quench in finite time. We establish the Kolmogorov scaling of the incompressible kinetic energy spectrum and demonstrate its universal scaling for different values of the quench time when rescaled by the nonequilibrium correlation length predicted by the Kibble-Zurek mechanism.

Kibble-Zurek dynamics of the BEC transition. To de-

scribe the non-equilibrium condensate dynamics and the emergence of SQT, we consider the 2D stochastic projected Gross-Pitaevskii equation [43–48]. This formalism has been widely used to model the BEC transition, with numerous studies demonstrating its quantitative agreement with experimental observations [31, 35]. Specifically, it describes the evolution of the low-energy coherent modes of a Bose gas via a complex order parameter Ψ_C , which evolves according to

$$d\Psi_C = \mathcal{P}_C [-(i + \gamma)(H_{sp} + g|\Psi_C|^2 - \mu)\Psi_C dt + d\eta], \quad (1)$$

where μ is the chemical potential, γ is the damping rate modeling energy dissipation due to the contact with the thermal bath, g is the coupling strength of the delta-function interaction between bosons, and $d\eta$ is a complex Gaussian noise increment accounting for thermal fluctuations. $H_{sp} = -(1/2)\nabla^2 + V(\mathbf{r})$ denotes the single-particle Hamiltonian, with $V(\mathbf{r})$ the external trapping potential. In this work, we focus on a periodic homogeneous system and set $V(\mathbf{r}) = 0$. Further details of Eq. (1) and its numerical implementation are provided in [49].

To drive the phase transition, we consider a linear quench of the chemical potential, $\mu(t) = \mu_i + (\mu_f - \mu_i)t/\tau_Q$, with μ_i and μ_f denoting its initial and final values, respectively. This protocol drives the system through the critical point μ_c at a finite rate τ_Q , resulting in the formation of a BEC populated with vortices. A vortex is characterized by a quantized circulation of the superfluid velocity, $\oint \mathbf{v}(\mathbf{r}, t) \cdot d\ell = (2\pi\hbar/m)w$, where $w \in \mathbb{Z}$ is the winding number. The associated singularity of the velocity field enforces a vanishing condensate density at the vortex center, with the healing length determining the core size. An example of a single realization of the newborn BEC is shown in Fig. 1, where vortices

can be recognized by the depletion of the BEC density at their core. The associated phase map indicates that only the values $w = \pm 1$ are generated in the course of the BEC transition. This is consistent with the fact that higher winding numbers are energetically costly and unstable against decay [50].

Using the mean-field values of the critical exponents $\nu = 1/2$ and $z = 2$, the KZM predicts the scaling of the freeze-out time, which sets the time scale in which the growth of the order parameter lags behind the crossing of the critical point set by the quench of $\mu(t)$. The equilibration time, when the growth of the number of bosons in BEC changes from exponential to linear [34, 37, 49], is proportional to the freeze-out time and scales universally as $t_{eq} \propto \hat{t} \propto \tau_Q^{1/2}$. This scaling is confirmed by the numerical results shown in the inset of Fig. 1 (c), where $t_{eq} = (3.779 \pm 0.693)\tau_Q^{0.541 \pm 0.069}$. At the equilibration time, the KZM further predicts that the vortex number scales as $n_v \propto \tau_Q^{-1/2}$, in agreement with the fit shown in Fig. 1 (c), where $n_v = (249.036 \pm 44.999)\tau_Q^{-0.534 \pm 0.047}$.

Compressible and incompressible energy spectra. By introducing the density-weighted velocity field $\mathbf{u}(\mathbf{r}) = |\Psi_C(\mathbf{r})|\mathbf{v}(\mathbf{r})$ [51–54], the kinetic energy of the newborn BEC takes the form $E = (m/2) \int |\mathbf{u}(\mathbf{r})|^2 d^2\mathbf{r}$. Using the canonical decomposition [51–54], \mathbf{u} can be separated into a compressible (irrotational) component \mathbf{u}_c , satisfying $\nabla \times \mathbf{u}_c = 0$, and an incompressible (solenoidal) component \mathbf{u}_i , for which $\nabla \cdot \mathbf{u}_i = 0$. The total kinetic energy is accordingly decomposed into its compressible and incompressible contributions,

$$E_{i,c} = \frac{m}{2} \int |\mathbf{u}_{i,c}(\mathbf{r})|^2 d^2\mathbf{r}. \quad (2)$$

It is particularly useful to express Eq. (2) in Fourier space, resulting in $E_{i,c} = \int E_{i,c}(k) dk$, with

$$E_{i,c}(k) := \frac{m}{2} k \int |\tilde{\mathbf{u}}_{i,c}(\mathbf{k})|^2 d\varphi_k, \quad (3)$$

where $\mathbf{k} = k(\cos \varphi_k, \sin \varphi_k)$ and $\tilde{\mathbf{u}}_{i,c}(\mathbf{k})$ the Fourier transform of $\mathbf{u}_{i,c}(\mathbf{r})$ [55].

Kolmogorov scaling of the energy spectrum in SQT. The occurrence of SQT in the newborn BEC is diagnosed by the Kolmogorov scaling of the incompressible kinetic energy spectrum $E_i(k)$ [15, 56], which has been experimentally measured in 2D BECs [18]. This law was originally derived for homogeneous isotropic turbulence where large eddies (with high Reynolds number) are continuously broken into smaller eddies (with small Reynolds number), and there exists a range of length scales (inertial range) where the details of energy injection and dissipation can be neglected and the eddies follow universal statistical properties [2, 57]. With the additional assumptions that, within this regime, the change of the kinetic energy per unit time is independent of k and the viscosity does not affect $E_i(k)$, di-

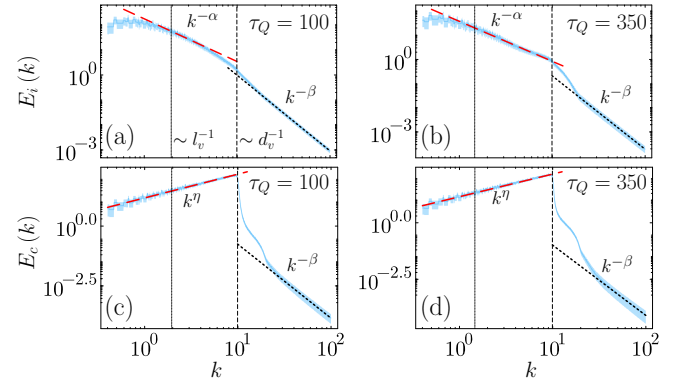


Figure 2. Incompressible and compressible kinetic energy spectra. Panels (a) and (b) show the incompressible kinetic energy spectrum $E_i(k)$ at the equilibration time following quenches with $\tau_Q = 100$ and $\tau_Q = 350$, respectively, each averaged over $\mathcal{R} = 1000$ independent noise realizations. The corresponding fitted power-law exponents are $\alpha = 1.710 \pm 0.079$, $\beta = 3.025 \pm 0.030$ for (a), and $\alpha = 1.654 \pm 0.031$, $\beta = 3.036 \pm 0.047$ for (b). Panels (c) and (d) display the compressible spectrum $E_c(k)$ for the same quench protocols, with fit parameters $(\eta, \beta) = (0.992 \pm 0.008, 3.090 \pm 0.110)$ and $(1.002 \pm 0.008, 3.111 \pm 0.223)$ respectively. The vertical dashed lines mark $k = 2\pi/d_v$, where $d_v = 4\xi_h$ gives a good estimate of the vortex diameter in our system, while the vertical dotted lines indicate $k = 2\pi/l_v$, with l_v being the mean nearest intervortex distance. Shaded error bands correspond to one standard deviation.

dimensional arguments imply a $k^{-5/3}$ scaling of the incompressible kinetic energy spectrum, independent of spatial dimensionality [57, 58]. This universal law is a direct reflection of the velocity-velocity autocorrelation function [2, 59]. At higher momenta, the inertial range over which the Kolmogorov scaling extends is interrupted by a second power law, $E_i(k) \propto k^{-3}$, that reflects the short-range properties of the vortex core and is thus unrelated to turbulence [55, 60]. As the radius of the vortex core is of the order of the condensate healing length $\xi_h := \sqrt{\hbar^2/2m\mu_f}$ [14, 60, 61], the inertial range lies below $k < 2\pi/\xi_h$. At large scales, it is further bounded by the mean intervortex distance l_v [55]. The width of this range is therefore determined by the quench speed, which sets the energy-injection scale through the universal KZ correlation length $\hat{\xi} \sim l_v$. As a result, the extent of the Kolmogorov scaling shrinks for faster quenches and broadens for moderate ones. This effect is illustrated in Fig. 2, showing the incompressible energy spectra at equilibration for quenches of duration $\tau_Q = 100$ in (a) and $\tau_Q = 350$ in (b). The corresponding fits yield $E_i(k) = (176.555 \pm 14.316)k^{-1.710 \pm 0.079}$, $E_i(k) = (1028.257 \pm 123.069)k^{-3.025 \pm 0.030}$ in panel (a), and $E_i(k) = (37.722 \pm 1.723)k^{-1.654 \pm 0.031}$, $E_i(k) = (226.968 \pm 42.383)k^{-3.036 \pm 0.047}$ in (b). The power-law fitted exponents in the inertial range are thus in agreement with the Kolmogorov scaling value $5/3 \simeq 1.67$

within the numerical uncertainty. In BECs the inertial range is typically narrow, spanning no more than one decade due to the lack of a wide separation between characteristic length scales [15, 54, 57]. This limitation can be mitigated by analyzing the velocity structure functions, which, due to their self-similar nature, allow the extension of the Kolmogorov scaling beyond the inertial range. In particular, in [49] we compute the longitudinal velocity increments $S_p(r) = \langle |[\mathbf{u}_i(\mathbf{R}+\mathbf{r}) - \mathbf{u}_i(\mathbf{R})] \cdot \mathbf{r}|^p \rangle$ and find clear power-law relations $S_p(r) \propto [S_3(r)]^{\zeta(p)}$, with exponents that deviate from the K41 prediction $\zeta(p) = p/3$ [1, 2, 18, 57, 59, 62–65], and are more accurately described by the refined K62 model [66]. While the KZM accurately describes the universal critical dynamics across the BEC transition, it does not account for other effects such as the annihilation of vortex-antivortex pairs, the losses of vortices at the edges of the trap, and coarsening. For slow quenches, the system evolves nearly adiabatically, resulting in suppressed vortex formation and diminished turbulence. As a consequence, the inertial range shrinks and the Kolmogorov scaling becomes less pronounced.

Although our main interest lies in the Kolmogorov scaling of the incompressible kinetic energy spectrum, we also plotted $E_c(k)$ at the equilibration time in Figs. 2 (c) and (d). For a 2D system at thermodynamic equilibrium, it is reported that $E_c(k) \propto k$ for small k [16]. In addition, since $E(k)$ follows the k^{-3} law at large k [52, 67], $E_c(k)$ is expected to follow the same power law. Our numerical results in Figs. 2 (c) and (d) are in agreement with these expectations.

Kibble-Zurek universality of SQT. Having established that the Kolmogorov scaling describes thermal quenches for two different values of τ_Q , we now demonstrate the nonequilibrium universality dictated by KZM in SQT. To this end, let us consider the total incompressible kinetic energy E_i . Since the density-weighted velocity field $\mathbf{u}_i = \sqrt{\rho} \mathbf{v}_i$ is concentrated around the vortex cores, E_i can be approximated as a sum of isolated vortex contributions, $E_i \simeq (m/2) n_v \int_{\mathcal{D}_{\hat{\xi}}} |\mathbf{u}_v(\mathbf{r})|^2 d^2 \mathbf{r}$, where

$|\mathbf{u}_v(\mathbf{r})| = \sqrt{\rho(\mathbf{r})} \hbar / (mr)$, and the integration domain $\mathcal{D}_{\hat{\xi}}$ is set by the KZ correlation length $\hat{\xi}$. At equilibration, the background density $\rho \simeq \mu(t_{eq})/g \propto \tau_Q^{-1/(1+z\nu)}$ and $\hat{\xi} \propto \tau_Q^{\nu/(1+z\nu)}$, so each vortex contributes $\int_{\mathcal{D}_{\hat{\xi}}} |\mathbf{u}_v|^2 d^2 \mathbf{r} \propto \tau_Q^{-1/(1+z\nu)}$ up to logarithmic corrections [49]. Combining this with the KZ vortex number scaling $n_v \propto \tau_Q^{-2\nu/(1+z\nu)}$ yields $E_i \propto \tau_Q^{-(1+2\nu)/(1+z\nu)}$ as confirmed numerically in [49]. Next, we consider the spectral density $E_i(k)$. Since the Kibble-Zurek length $\hat{\xi}$ sets the characteristic momentum scale at equilibration, it is natural to assume the scaling ansatz $E_i(k; \tau_Q) = A(\tau_Q) F(k\hat{\xi})$, where F encodes the spectral shape and $A(\tau_Q)$ is a k -independent amplitude. Using $E_i \propto \tau_Q^{-(1+2\nu)/(1+z\nu)}$ together with

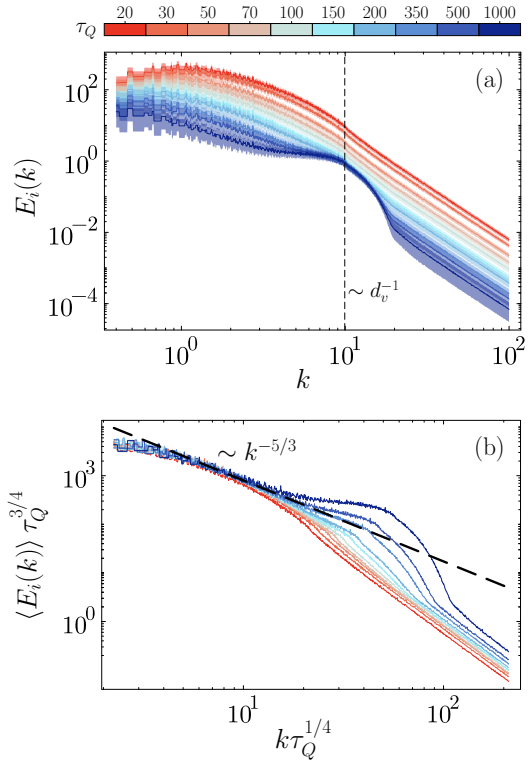


Figure 3. Kibble-Zurek universality of the incompressible kinetic energy spectrum. Panel (a) shows $E_i(k)$ at equilibration time for various τ_Q values, each averaged over $\mathcal{R} = 1000$ stochastic realizations. The dashed vertical line marks $k = 2\pi/d_v$ with the vortex diameter estimated to be $d_v = 4\xi_h$. Panel (b) displays $\langle E_i(k) \rangle \tau_Q^{3/4}$ as a function of the scaled momentum $k\tau_Q^{1/4} \propto k\xi$. Shaded error bands indicate one standard deviation in (a) and 95% confidence interval in (b).

$\hat{\xi} \propto \tau_Q^{\nu/(1+z\nu)}$ gives $A(\tau_Q) \propto \tau_Q^{-(1+\nu)/(1+z\nu)}$, implying a collapse of the spectra across different quench rates under the rescaling

$$k \rightarrow k \tau_Q^{\nu/(1+z\nu)}, \quad E_i(k) \rightarrow E_i(k) \tau_Q^{(1+\nu)/(1+z\nu)}, \quad (4)$$

as shown in Fig. 3 for the mean-field values of the critical exponents. A universal collapse also emerges for the compressible spectrum $E_c(k)$, under a distinct rescaling, at low temperature where phonon emission from vortex-antivortex annihilation dominates over thermal density fluctuations (see [49] for details). In addition, for k exceeding d_v^{-1} , the lack of collapse for $E_i(k)$ when rescaled by the KZ variables in the k^{-3} scaling regime is expected as it is governed by an equilibrium quantity, the vortex core radius, that is independent of the quench rate.

Deviations from the universal collapse can also be expected for fast quenches (e.g., $\tau_Q \leq 10$), for which the KZM breaks down [36, 68] due to the saturation of the defect density shown in Fig. 1 (c). However, such deviations may be taken into account by using the associ-

ated correlation length and energy scale, which scale universally with the quench depth rather than the quench time. Naturally, other non-universal processes beyond KZM and its extensions, governing the evolution after the formation of the BEC, such as atom losses, vortex-antivortex annihilation and coarsening, are expected to suppress the Kolmogorov scaling and SQT.

Discussion and conclusion. In summary, we have shown that superfluid formation triggered by a finite-time quench gives rise to SQT. To this end, we have established that the incompressible kinetic energy of the emergent nonequilibrium BEC exhibits Kolmogorov scaling with respect to the wavevector. Moreover, using the nonequilibrium correlation length predicted by KZM and the associated energy scale, we have shown that the Kolmogorov scaling admits a universal collapse for different values of the quench time. Our findings highlight the rich interplay between distinct yet complementary notions of universality: the universal scaling of energy spectra in turbulent flows and the universal defect dynamics across continuous phase transitions.

Note. During the completion of this work, Ref. [69] reported the study of a 4D superfluid with Kolmogorov scaling for the total energy, rather than the incompressible energy in the 2D case we discuss.

Acknowledgments. MM is grateful to András Grabarits, Simon Fisher, Martin Gažo, and Zoran Hadžibabic for valuable discussions. SS would like to further thank Sol Kim and Yong-il Shin for insightful comments, and the Institut d’Études Scientifiques de Cargèse, for support and hospitality during the program **Bridges over turbulent matters - Navigating across observations, concepts and models**. The authors acknowledge financial support from the Luxembourg National Research Fund under Grant No. C22/MS/17132060/BeyondKZM. MT would like to thank Anusandhan National Research Foundation (ANRF), Government of India, for the financial support through the Prime Minister Early Career Research Grant with Grant No. ANRF/ECRG/2024/003150/PMS, and Christ University for funding the research through the seed grant, sanction No. CU-ORS-SM-24/94. The numerical simulations presented in this work were carried out using the HPC resources of the University of Luxembourg (ULHPC).

Data Availability. The data that support the findings of this article are openly available [70].

- [2] U. Frisch, *Turbulence: The Legacy of A. N. Kolmogorov* (Cambridge University Press, Cambridge, 1995).
- [3] R. Feynman, “Chapter ii application of quantum mechanics to liquid helium,” (Elsevier, 1955) pp. 17–53.
- [4] N. G. Berloff and B. V. Svistunov, “Scenario of strongly nonequilibrated bose-einstein condensation,” *Phys. Rev. A* **66**, 013603 (2002).
- [5] M. Kobayashi and M. Tsubota, “Kolmogorov spectrum of superfluid turbulence: Numerical analysis of the gross-pitaevskii equation with a small-scale dissipation,” *Phys. Rev. Lett.* **94**, 065302 (2005).
- [6] M. Tsubota, *Progress in Low Temperature Physics: Quantum Turbulence*, ISSN (Elsevier Science, 2008).
- [7] H. Salman and N. G. Berloff, “Condensation of classical nonlinear waves in a two-component system,” *Physica D: Nonlinear Phenomena* **238**, 1482 (2009).
- [8] M. C. Tsatsos, P. E. Tavares, A. Cidrim, A. R. Fritsch, M. A. Caracanhas, F. E. A. dos Santos, C. F. Barenghi, and V. S. Bagnato, “Quantum turbulence in trapped atomic Bose-Einstein condensates,” *Physics Reports* **622**, 1 (2016).
- [9] H. Salman and D. Maestrini, “Long-range ordering of topological excitations in a two-dimensional superfluid far from equilibrium,” *Phys. Rev. A* **94**, 043642 (2016).
- [10] M. T. Wheeler, H. Salman, and M. O. Borgh, “Relaxation dynamics of half-quantum vortices in a two-dimensional two-component bose-einstein condensate,” *Europhysics Letters* **135**, 30004 (2021).
- [11] P. Nandy, A. S. Matsoukas-Roubeas, P. Martínez-Azcona, A. Dymarsky, and A. del Campo, “Quantum dynamics in krylov space: Methods and applications,” *Physics Reports* **1125**, 1 (2025).
- [12] M. Ueda, *Fundamentals and New Frontiers of Bose-Einstein Condensation* (World Scientific, 2010).
- [13] I. Carusotto and C. Ciuti, “Quantum fluids of light,” *Rev. Mod. Phys.* **85**, 299 (2013).
- [14] L. Pitaevskii and S. Stringari, *Bose-Einstein Condensation*, International Series of Monographs on Physics (Clarendon Press, Oxford, 2003).
- [15] M. Tsubota, M. Kobayashi, and H. Takeuchi, “Quantum hydrodynamics,” *Physics Reports* **522**, 191 (2013).
- [16] R. Numasato, M. Tsubota, and V. S. L’vov, “Direct energy cascade in two-dimensional compressible quantum turbulence,” *Phys. Rev. A* **81**, 063630 (2010).
- [17] P. M. Chesler, H. Liu, and A. Adams, “Holographic vortex liquids and superfluid turbulence,” *Science* **341**, 368 (2013).
- [18] M. Zhao, J. Tao, and I. B. Spielman, “Kolmogorov scaling in turbulent 2d bose-einstein condensates,” *Phys. Rev. Lett.* **134**, 083402 (2025).
- [19] S. W. Seo, B. Ko, J. H. Kim, and Y. Shin, “Observation of vortex-antivortex pairing in decaying 2d turbulence of a superfluid gas,” *Scientific Reports* **7**, 4587 (2017).
- [20] G. Gauthier, M. T. Reeves, X. Yu, A. S. Bradley, M. A. Baker, T. A. Bell, H. Rubinsztein-Dunlop, M. J. Davis, and T. W. Neely, “Giant vortex clusters in a two-dimensional quantum fluid,” *Science* **364**, 1264 (2019).
- [21] R. Panico, P. Comaron, M. Matuszewski, A. S. Lanotte, D. Trypogeorgos, G. Gigli, M. D. Giorgi, V. Ardizzone, D. Sanvitto, and D. Ballarini, “Onset of vortex clustering and inverse energy cascade in dissipative quantum fluids,” *Nature Photonics* **17**, 451 (2023).
- [22] W. J. Kwon, G. Moon, J.-y. Choi, S. W. Seo, and Y.-i. Shin, “Relaxation of superfluid turbulence in highly

* seongho.shin@uni.lu

† matteo.massaro@uni.lu

[1] A. Kolmogorov, “The Local Structure of Turbulence in Incompressible Viscous Fluid for Very Large Reynolds’ Numbers,” *Akademiiia Nauk SSSR Doklady* **30**, 301 (1941).

oblate bose-einstein condensates,” *Phys. Rev. A* **90**, 063627 (2014).

[23] M. T. Reeves, K. Goddard-Lee, G. Gauthier, O. R. Stockdale, H. Salman, T. Edmonds, X. Yu, A. S. Bradley, M. Baker, H. Rubinsztein-Dunlop, M. J. Davis, and T. W. Neely, “Turbulent relaxation to equilibrium in a two-dimensional quantum vortex gas,” *Phys. Rev. X* **12**, 011031 (2022).

[24] T. W. B. Kibble, “Topology of cosmic domains and strings,” *Journal of Physics A: Mathematical and General* **9**, 1387 (1976).

[25] T. Kibble, “Some implications of a cosmological phase transition,” *Physics Reports* **67**, 183 (1980).

[26] W. H. Zurek, “Cosmological experiments in superfluid helium?” *Nature* **317**, 505 (1985).

[27] W. H. Zurek, “Cosmic strings in laboratory superfluids and the topological remnants of other phase transitions,” *Acta Physica Polonica B* **24**, 1301 (1993).

[28] A. del Campo and W. H. Zurek, “Universality of phase transition dynamics: Topological defects from symmetry breaking,” *Int. J. Mod. Phys. A* **29**, 1430018 (2014).

[29] B. Damski and W. H. Zurek, “Soliton creation during a bose-einstein condensation,” *Phys. Rev. Lett.* **104**, 160404 (2010).

[30] G. Lamporesi, S. Donadello, S. Serafini, F. Dalfovo, and G. Ferrari, “Spontaneous creation of Kibble-Zurek solitons in a Bose-Einstein condensate,” *Nature Physics* **9**, 656 (2013).

[31] C. N. Weiler, T. W. Neely, D. R. Scherer, A. S. Bradley, M. J. Davis, and B. P. Anderson, “Spontaneous vortices in the formation of Bose-Einstein condensates,” *Nature* **455**, 948 (2008).

[32] L. Chomaz, L. Corman, T. Bienaimé, R. Desbuquois, C. Weitenberg, S. Nascimbène, J. Beugnon, and J. Dalibard, “Emergence of coherence via transverse condensation in a uniform quasi-two-dimensional Bose gas,” *Nat. Comm.* **6**, 6162 (2015).

[33] A. del Campo, A. Retzker, and M. B. Plenio, “The inhomogeneous kibble-zurek mechanism: vortex nucleation during bose-einstein condensation,” *New Journal of Physics* **13**, 083022 (2011).

[34] P. M. Chesler, A. M. García-García, and H. Liu, “Defect formation beyond kibble-zurek mechanism and holography,” *Phys. Rev. X* **5**, 021015 (2015).

[35] I.-K. Liu, J. Dziarmaga, S.-C. Gou, F. Dalfovo, and N. P. Proukakis, “Kibble-zurek dynamics in a trapped ultracold bose gas,” *Phys. Rev. Res.* **2**, 033183 (2020).

[36] H.-B. Zeng, C.-Y. Xia, and A. del Campo, “Universal breakdown of kibble-zurek scaling in fast quenches across a phase transition,” *Phys. Rev. Lett.* **130**, 060402 (2023).

[37] M. Thudiyangal and A. del Campo, “Universal vortex statistics and stochastic geometry of bose-einstein condensation,” *Phys. Rev. Res.* **6**, 033152 (2024).

[38] M. T. Wheeler, H. Salman, and M. O. Borgh, “Dynamics of a nonequilibrium discontinuous quantum phase transition in a spinor bose-einstein condensate,” *Communications Physics* **8**, 153 (2025).

[39] W. Kirkby, H. Salman, T. Gasenzer, and L. Chomaz, “Kibble-zurek scaling of the superfluid-supersolid transition in an elongated dipolar gas,” *Phys. Rev. Res.* **7**, 023248 (2025).

[40] N. Navon, A. L. Gaunt, R. P. Smith, and Z. Hadzibabic, “Critical dynamics of spontaneous symmetry breaking in a homogeneous Bose gas,” *Science* **347**, 167 (2015).

[41] B. Ko, J. W. Park, and Y. Shin, “Kibble-zurek universality in a strongly interacting fermi superfluid,” *Nature Physics* **15**, 1227 (2019).

[42] M. Kim, T. Rabga, Y. Lee, J. Goo, D. Bae, and Y. Shin, “Suppression of spontaneous defect formation in inhomogeneous bose gases,” *Phys. Rev. A* **106**, L061301 (2022).

[43] C. W. Gardiner and M. J. Davis, “The stochastic gross-pitaevskii equation: Ii,” *Journal of Physics B: Atomic, Molecular and Optical Physics* **36**, 4731 (2003).

[44] P. B. Blakie, A. S. Bradley, M. J. Davis, R. J. Ballagh and C. W. Gardiner, “Dynamics and statistical mechanics of ultra-cold Bose gases using c-field techniques,” *Advances in Physics* **57**, 363 (2008).

[45] S. J. Rooney, P. B. Blakie, and A. S. Bradley, “Stochastic projected gross-pitaevskii equation,” *Phys. Rev. A* **86**, 053634 (2012).

[46] S. J. Rooney, P. B. Blakie, and A. S. Bradley, “Numerical method for the stochastic projected gross-pitaevskii equation,” *Phys. Rev. E* **89**, 013302 (2014).

[47] A. S. Bradley, S. J. Rooney, and R. G. McDonald, “Low-dimensional stochastic projected gross-pitaevskii equation,” *Phys. Rev. A* **92**, 033631 (2015).

[48] R. G. McDonald, P. S. Barnett, F. Atayee, and A. S. Bradley, “Dynamics of hot Bose-Einstein condensates: stochastic Ehrenfest relations for number and energy damping,” *SciPost Phys.* **8**, 029 (2020).

[49] url will be inserted by publisher, .

[50] M. Tsubota, “Quantum turbulence,” *Journal of the Physical Society of Japan* **77**, 111006 (2008).

[51] C. Nore, M. Abid, and M. E. Brachet, “Kolmogorov turbulence in low-temperature superflows,” *Phys. Rev. Lett.* **78**, 3896 (1997).

[52] C. Nore, M. Abid, and M. E. Brachet, “Decaying kolmogorov turbulence in a model of superflow,” *Physics of Fluids* **9**, 2644 (1997).

[53] S.-i. Ogawa, M. Tsubota, and Y. Hattori, “Study of reconnection and acoustic emission of quantized vortices in superfluid by the numerical analysis of the gross-pitaevskii equation,” *Journal of the Physical Society of Japan* **71**, 813 (2002).

[54] M. Kobayashi and M. Tsubota, “Kolmogorov spectrum of quantum turbulence,” *Journal of the Physical Society of Japan* **74**, 3248 (2005).

[55] A. S. Bradley and B. P. Anderson, “Energy spectra of vortex distributions in two-dimensional quantum turbulence,” *Phys. Rev. X* **2**, 041001 (2012).

[56] T. W. Neely, A. S. Bradley, E. C. Samson, S. J. Rooney, E. M. Wright, K. J. H. Law, R. Carretero-González, P. G. Kevrekidis, M. J. Davis, and B. P. Anderson, “Characteristics of two-dimensional quantum turbulence in a compressible superfluid,” *Phys. Rev. Lett.* **111**, 235301 (2013).

[57] C. F. Barenghi, L. Skrbek, and K. R. Sreenivasan, *Quantum Turbulence* (Cambridge University Press, Cambridge, 2023).

[58] W. F. Vinen and J. J. Niemela, “Quantum turbulence,” *Journal of Low Temperature Physics* **128**, 167 (2002).

[59] A. N. Kolmogorov, “Dissipation of Energy in Locally Isotropic Turbulence,” *Akademii Nauk SSSR Doklady* **32**, 16 (1941).

[60] T. Tanogami, “Theoretical analysis of quantum turbulence using the onsager ideal turbulence theory,” *Phys. Rev. E* **103**, 023106 (2021).

[61] V. L. Ginzburg and L. P. Pitaevskii, “On the theory of

superfluidity,” Sov. Phys. JETP **7**, 858 (1958).

[62] R. Benzi, S. Ciliberto, R. Tripiccione, C. Baudet, F. Massaioli, and S. Succi, “Extended self-similarity in turbulent flows,” Phys. Rev. E **48**, R29 (1993).

[63] B. Dubrulle, “Intermittency in fully developed turbulence: Log-poisson statistics and generalized scale covariance,” Phys. Rev. Lett. **73**, 959 (1994).

[64] S. Ciliberto, “Extended self similarity,” in *Turbulence: A Tentative Dictionary*, edited by P. Tabeling and O. Cardoso (Springer US, Boston, MA, 1994) pp. 27–30.

[65] G. Krstulovic, “Grid superfluid turbulence and intermittency at very low temperature,” Phys. Rev. E **93**, 063104 (2016).

[66] A. N. Kolmogorov, “A refinement of previous hypotheses concerning the local structure of turbulence in a viscous incompressible fluid at high reynolds number,” Journal of Fluid Mechanics **13**, 82 (1962).

[67] G. Krstulovic and M. Brachet, “Comment on “superfluid turbulence from quantum kelvin wave to classical kolmogorov cascades”,” Phys. Rev. Lett. **105**, 129401 (2010).

[68] C.-Y. Xia, H.-B. Zeng, A. Grabarits, and A. del Campo, “Kibble-zurek mechanism and beyond: Lessons from a holographic superfluid disk,” (2024), arXiv:2406.09433 [cond-mat.stat-mech].

[69] W. can Yang, “Non-equilibrium dynamics and universality of 4d quantum vortices and turbulence,” (2025), arXiv:2504.04409 [cond-mat.quant-gas].

[70] S.-H. Shinn, M. Massaro, M. THUDIYANGAL, and A. del Campo, “Spontaneous quantum turbulence in a newborn bose- einstein condensate via the kibble-zurek mechanism data,” (2025).

[71] C. Rackauckas and Q. Nie, “DifferentialEquations.jl - A Performant and Feature-Rich Ecosystem for Solving Differential Equations in Julia,” Journal of Open Research Software (2017), 10.5334/jors.151.

[72] C. Rackauckas and Q. Nie, “Adaptive methods for stochastic differential equations via natural embeddings and rejection sampling with memory,” Discrete and Continuous Dynamical Systems - B **22**, 2731 (2017).

[73] C. Rackauckas and Q. Nie, “Stability-optimized high order methods and stiffness detection for pathwise stiff stochastic differential equations,” in *2020 IEEE High Performance Extreme Computing Conference (HPEC)* (2020) pp. 1–8.

[74] O. Penrose and L. Onsager, “Bose-einstein condensation and liquid helium,” Phys. Rev. **104**, 576 (1956).

[75] A. Villois, G. Krstulovic, D. Proment, and H. Salman, “A vortex filament tracking method for the gross-pitaevskii model of a superfluid,” Journal of Physics A: Mathematical and Theoretical **49**, 415502 (2016).

[76] K. Watanabe, *Integral Transform Techniques for Green’s Function*, Lecture Notes in Applied and Computational Mechanics (Springer International Publishing Switzerland, Cham, 2015).

[77] M. Frigo and S. G. Johnson, “The design and implementation of FFTW3,” Proceedings of the IEEE **93**, 216 (2005), special issue on “Program Generation, Optimization, and Platform Adaptation”.

—Supplementary Material—

Spontaneous Quantum Turbulence in a Newborn Bose-Einstein Condensate via the Kibble-Zurek Mechanism

Seong-Ho Shinn^{1,*}, Matteo Massaro^{2,†}, Mithun Thudiyangal^{3,4} and Adolfo del Campo^{2,5}

¹*Department of Physics and Materials Science, University of Luxembourg, L-1511 Luxembourg, Luxembourg*

²*Department of Physics and Materials Science, University of Luxembourg, L-1511 Luxembourg, Luxembourg*

³*Center for Quantum Technologies and Complex Systems (CQTCS),
Christ University, Bengaluru, Karnataka 560029, India*

⁴*Department of Physics and Electronics, Christ University, Bengaluru, Karnataka 560029, India*

⁵*Donostia International Physics Center, E-20018 San Sebastián, Spain*

TWO-DIMENSIONAL STOCHASTIC PROJECTED GROSS-PITAEVSKII EQUATION

The stochastic projected Gross-Pitaevskii equation (SPGPE) is a description based on c -field methods [44], consisting of dividing the system's modes into a coherent region (\mathcal{C}), which includes the low-lying, highly populated levels, and an incoherent region of high-energy, sparsely occupied states that act as a thermal reservoir. The evolution of \mathcal{C} is captured by a classical field $\Psi_{\mathcal{C}}$, which evolves according to

$$d\Psi_{\mathcal{C}} = \mathcal{P}_{\mathcal{C}} \left[-(i + \gamma) (H_{sp} + g|\Psi_{\mathcal{C}}|^2 - \mu(t)) \Psi_{\mathcal{C}} dt + d\eta \right], \quad (\text{S1})$$

where length, time, and temperature are measured in units of $l := \sqrt{\hbar^2/mE_{sc}}$, \hbar/E_{sc} , and E_{sc}/k_B , respectively. Here E_{sc} sets the energy scale, m is the mass of a boson, \hbar the reduced Planck constant, k_B the Boltzmann constant, μ the chemical potential, γ the dissipation rate, $g = 2\sqrt{2\pi}a_s/l_{\perp}$ the coupling strength of the repulsive delta-function interaction between bosons in a quasi-two-dimensional system [14, 47], with a_s the s-wave scattering length and $l_{\perp} = \sqrt{\hbar/(mw_{\perp})}$ the harmonic-oscillator length associated with the transverse confinement. $H_{sp} = -(1/2)\nabla^2 + V(\mathbf{r})$ denotes the single-particle Hamiltonian, and its eigenfunctions $\phi_n(\mathbf{r})$ serve as a convenient basis to describe the \mathcal{C} region. The noise term $d\eta$ is a complex Wiener process, with an autocorrelation function proportional to the temperature T . Specifically, it satisfies

$$\langle d\eta(\mathbf{r}, t) \rangle = 0, \quad \langle d\eta(\mathbf{r}, t) d\eta^*(\mathbf{r}', t) \rangle = 2T\gamma \delta_{\mathcal{C}}(\mathbf{r} - \mathbf{r}') dt, \quad (\text{S2})$$

where $\delta_{\mathcal{C}}(\mathbf{r} - \mathbf{r}') = \sum_{n \in \mathcal{C}} \phi_n(\mathbf{r}) \phi_n^*(\mathbf{r}')$ is the delta function restricted to the low-energy subspace. This subspace is spanned by the set of eigenfunctions $\{\phi_n\}_{n \in \mathcal{C}}$ with energies ϵ_n below a properly chosen cut-off ϵ_{cut} . Finally, $\mathcal{P}_{\mathcal{C}}$ denotes the projector operator, which restricts the dynamics to the low-energy subspace. Specifically, $\mathcal{P}_{\mathcal{C}}$ acts on a generic field $f(\mathbf{r})$ by projecting it onto the \mathcal{C} region [44]:

$$\mathcal{P}_{\mathcal{C}} f(\mathbf{r}) = \sum_{n: \epsilon_n < \epsilon_{cut}} \phi_n(\mathbf{r}) \int f(\mathbf{r}') \phi_n^*(\mathbf{r}') d^2\mathbf{r}'. \quad (\text{S3})$$

The action of the projector is thus naturally implemented in the eigenbasis of the single-particle Hamiltonian H_{sp} , by setting a maximum eigenmode and ensuring that the dynamics does not develop components above this cutoff. The field $\Psi_{\mathcal{C}}$ is then conveniently represented as a sum over the corresponding basis states

$$\Psi_{\mathcal{C}}(\mathbf{r}, t) = \sum_{n \in \mathcal{C}} c_n(t) \phi_n(\mathbf{r}), \quad (\text{S4})$$

with the weights c_n encoding the particle occupation number in the n -th mode. Substituting this expansion into (S1) yields the evolution equations for the coefficients c_n . To integrate these equations numerically, we rely on the Julia library `DifferentialEquations.jl` [71], employing a stability-optimized stochastic Runge-Kutta algorithm (SOSRA) for time propagation [72, 73]. The simulations are performed in a periodic $L \times L$ homogeneous box (i.e., $V(\mathbf{r}) = 0$), with $\Psi_{\mathcal{C}} = 0$ as the initial condition. The system is then relaxed for t_r time units before beginning the quench. Unless otherwise specified, we use the parameter values in Table S1, motivated by the choices in [37].

Table S1. Simulation parameters

L	t_r	μ_i	μ_f	g	γ	T	ϵ_{cut}
30	10	0.1	20	1	0.03	1	$2.5 \mu_f$

Determination of the equilibration time

The equilibration time t_{eq} is identified by analyzing the time evolution of the norm of the order parameter, $N_C/L^2 = (1/L^2) \int |\Psi_C(\mathbf{r}, t)|^2 d^2\mathbf{r}$. In the spirit of [34], we locate the global maximum of $d^2(N_C/L^2)/dt^2$ and identify the subsequent interval (t_1, t_2) where $d^2(N_C/L^2)/dt^2 \leq -\Delta$, with Δ set to 10% of the maximum. We then take $t_{\text{eq}} = t_2$. The procedure is illustrated in Fig. S1.

The equilibration time measured from the critical crossing scales with the Kibble-Zurek (KZ) freeze-out time as

$$\bar{t}_{\text{eq}} := t_{\text{eq}} - t_c \propto \hat{t} \propto \tau_Q^{z\nu/(1+z\nu)}, \quad (\text{S5})$$

where $t_c = \tau_Q(\mu_c - \mu_i)/(\mu_f - \mu_i)$ denotes the time at which the system crosses the critical point, and $\mu_c := \mu(t_c)$ is the corresponding value of the chemical potential. This universal scaling is confirmed in the mean-field regime by the numerical results presented in the main text, which yield

$$t_{\text{eq}} = (3.779 \pm 0.693) \tau_Q^{0.541 \pm 0.069} + (0.078 \pm 0.059) \tau_Q. \quad (\text{S6})$$

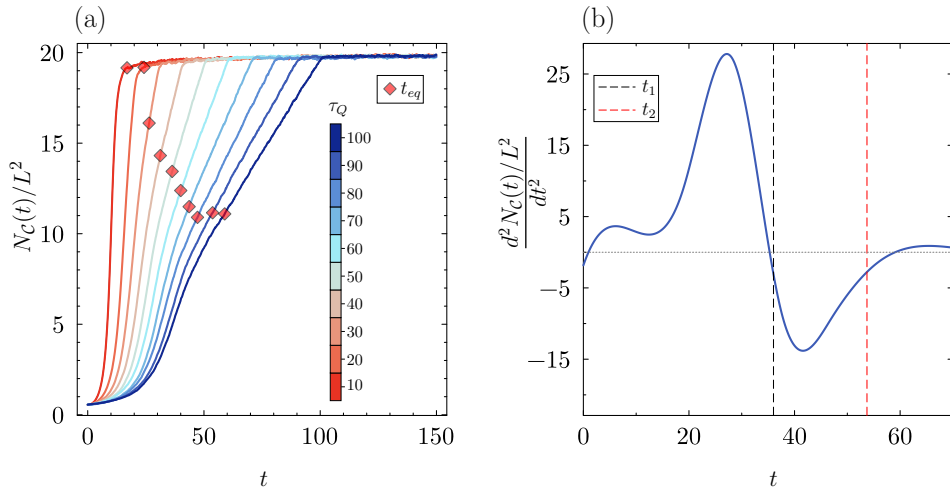


Figure S1. Determination of the equilibration time. Panel (a) shows the time evolution of the C -region number density (i.e., $N_C(t)/L^2 = (1/L^2) \int |\Psi_C(\mathbf{r}, t)|^2 d^2\mathbf{r}$) for quench times τ_Q from 10 to 100. The equilibration time t_{eq} is determined by considering the second derivative of N_C/L^2 and identifying the time interval $t_1 \leq t \leq t_2$ such that $d^2(N_C/L^2)(t)/dt^2 \leq -\Delta$ for $t_1 \leq t \leq t_2$. In particular, we set Δ to be 10% of the maximum value of $d^2(N_C/L^2)(t)/dt^2$. This is shown for the case $\tau_Q = 90$ in panel (b). Finally, the equilibration time is defined as $t_{\text{eq}} = t_2$.

Condensate fraction

Within the SPGPE description, the condensate fraction (defined as the ratio between the number of bosons in the Bose-Einstein condensate (BEC) state and the total number of bosons in the system) can be computed efficiently by means of the Penrose-Onsager criterion [74]. In particular, the occupation N_0 of the condensate mode is given by the largest eigenvalue of the single-particle density matrix

$$\rho(\mathbf{r}, \mathbf{r}') = \langle \Psi_C(\mathbf{r}) \Psi_C^*(\mathbf{r}') \rangle, \quad (\text{S7})$$

where $\langle \cdot \rangle$ denotes the ensemble average. In practice, this quantity is most conveniently evaluated in the eigenmode basis of the single-particle Hamiltonian [44]. The condensate fraction is then computed as N_0/N_{tot} , where N_{tot} denotes

the total number of bosons in the system. Specifically, $N_{\text{tot}} = N_{\mathcal{C}} + N_{\mathcal{I}}$, with $N_{\mathcal{C}} = \int |\Psi_{\mathcal{C}}(\mathbf{r})|^2 d^2\mathbf{r}$ the population of the coherent (\mathcal{C}) low-energy sector, and $N_{\mathcal{I}}$ the number of thermal bosons belonging to the incoherent (\mathcal{I}) high-energy region. The atoms in \mathcal{I} are assumed to be non-interacting and thermalized, and their number can therefore be determined using the Bose-Einstein distribution [35]. Fig. S2 shows that the condensate fraction increases as the quench speed decreases, consistent with slower quenches generating fewer excitations and resulting in a more coherent condensate at the end of the quench (for reference, $N_0(\tau_Q)/N_{\text{tot}}(\tau_Q) = 0.945 \pm 0.024$ for $\tau_Q = 1000$, averaged over 100 stochastic realizations). We also note that for quench times τ_Q below a threshold lying between 20 and 30, the quench is rapid enough that the equilibration time exceeds the quench duration. Consequently, for these τ_Q values the condensate fraction is larger at t_{eq} than at $t = \tau_Q$.

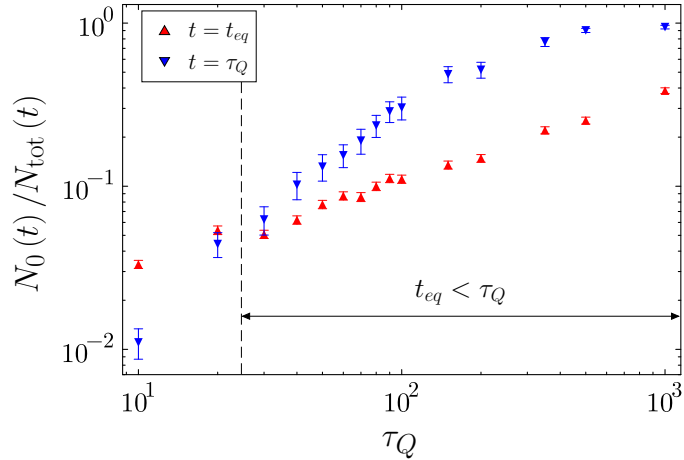


Figure S2. **Condensate fraction at $t = t_{eq}$ and $t = \tau_Q$.** The condensate fraction is shown at equilibration time t_{eq} and at the end of the quench ($t = \tau_Q$). The values at t_{eq} are averaged over $\mathcal{R} = 1000$ stochastic realizations (same dataset as in the main text), while those at $t = \tau_Q$ are averaged over $\mathcal{R} = 100$ realizations. Error bars denote 95% confidence interval.

Vortex detection algorithm

To determine the positions of the vortex cores at equilibration time, we locate the zeros of the condensate density $\rho_{\mathcal{C}}(\mathbf{r}, t_{eq}) = |\Psi_{\mathcal{C}}(\mathbf{r}, t_{eq})|^2$ and check the associated winding number. Specifically, we discretize the $L \times L$ system onto a $N_g \times N_g$ grid, with $N_g = 3000$, and identify each lattice site where $\rho_{\mathcal{C}}(\mathbf{r}, t_{eq})$ has a local minimum with value below $0.1\mu_f/g$. Starting from these initial guesses, we refine the locations of the zeros of $\rho_{\mathcal{C}}$ by iteratively applying the Newton-Raphson algorithm, until the condition $\rho_{\mathcal{C}}(\mathbf{r}) \leq 10^{-5}$ is fulfilled [75]. For each vortex candidate position, we calculate the winding number by integrating the superfluid velocity along a circle of radius $r_{\text{test}} = 0.06\xi_h$ centered on it, confirming whether it is a true vortex core.

VELOCITY STRUCTURE FUNCTIONS ANALYSIS AND EXTENDED SELF-SIMILARITY

In the main text, we have shown that a BEC created via a thermal quench develops a turbulent superfluid state characterized by the celebrated $k^{-5/3}$ Kolmogorov scaling in the incompressible kinetic energy spectrum. This power law holds within the inertial range (IR), corresponding to wavenumbers associated with length scales between the typical nearest inter-vortex separation (which sets the energy injection scale controlled by the quench rate) and the vortex core size, beyond which the spectrum reflects the static vortex structure rather than turbulence. The extent of this range usually spans about one decade in k or less, depending on the quench rate, reflecting the limited separation of characteristic length scales in atomic BECs. In particular, the ratio of the system size L to the healing length ξ_h is typically $L/\xi_h \sim O(70)$ in experiments [32], while in our simulation it is $L/\xi_h = 30\sqrt{2\mu_f} = 189.737$. To mitigate this limitation and obtain a broader scaling regime, we resort to the principle of extended self-similarity of the velocity structure functions. In particular, we consider the p -th order longitudinal velocity structure function $S_p(r)$, defined

as

$$S_p(r) = \langle |[\mathbf{u}_i(\mathbf{R} + \mathbf{r}) - \mathbf{u}_i(\mathbf{R})] \cdot \mathbf{e}_r|^p \rangle, \quad (\text{S8})$$

where \mathbf{u}_i denotes the incompressible component of the weighted velocity introduced in the main text, and \mathbf{e}_r is the unit vector along \mathbf{r} . The brackets $\langle \cdot \rangle$ indicate averaging over all possible system positions \mathbf{R} and orientations of \mathbf{e}_r . In the IR, Kolmogorov's 1941 (K41) theory predicts the power-law $S_p(r) \propto r^{\zeta(p)}$, with $\zeta(p) = p/3$. For $p = 2$, this scaling relation yields the incompressible kinetic energy spectrum $E_i(k) \propto k^{-5/3}$ [2, 59, 62, 63]. In Fig. S3 (a), we show the structure functions $S_p(r)$ up to order $p = 5$. The Kolmogorov power-law regime appears narrow, making it difficult to reliably extract the scaling exponents. To overcome this, we additionally plot S_p as a function of S_3 in Fig. S3 (c)-(f). Since $S_3 \propto r$ according to K41, this representation preserves the same scaling exponents as $S_p(r)$. Moreover, the scaling law extends beyond the IR, revealing the self-similar character of the velocity structure functions, known as extended self-similarity (ESS) [62]. In particular, Fig. S3 demonstrates that the relation

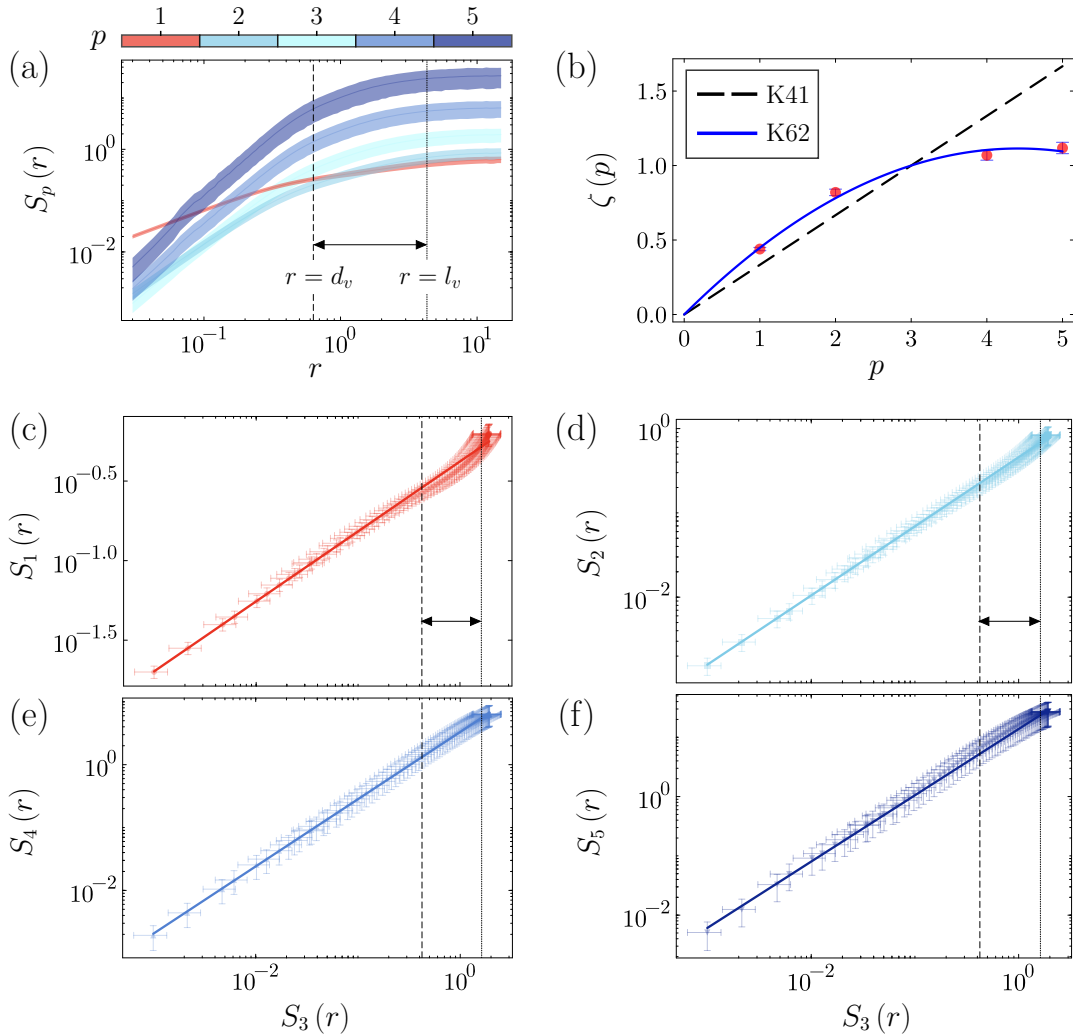


Figure S3. Velocity structure functions and extended self-similarity. (a) Velocity structure functions $S_p(r)$ at equilibration time for a quench of duration $\tau_Q = 350$ at temperature $T = 1$, averaged over $\mathcal{R} = 1000$ independent noise realizations. Here, the vertical lines mark the mean nearest inter-vortex distance l_v , and the vortex diameter $d_v = 4\xi_h$, with ξ_h being the healing length. (b) Scaling exponents $\zeta(p)$ obtained from the relation $S_p(r) \propto [S_3(r)]^{\zeta(p)}$. (c - f) $S_p(r)$ as a function of $S_3(r)$, where the vertical lines delimit the region $S_3(d_v) \leq S_3(r) \leq S_3(l_v)$. Solid lines are fits with $S_p(r) \propto [S_3(r)]^{\zeta(p)}$ where the fitted values of $\zeta(p)$ are the ones shown in (b). In all panels except (b), error bands and error bars represent one standard deviation. In panel (b), $\zeta(p)$ is computed by accounting for uncertainties in both $S_p(r)$ and $S_3(r)$, and the resulting error bars indicate the standard errors (i.e., the square roots of the diagonal elements of the covariance matrix) obtained from the orthogonal distance regression.

$S_p(r) \propto [S_3(r)]^{\zeta(p)}$ holds well beyond the inertial range for $\tau_Q = 350$, namely over $0.03 \lesssim r \lesssim l_v = 4.295$, while the corresponding inertial range lies within $d_v = 0.632 \lesssim r \lesssim l_v$ (see Fig. 2(b) in the main text). The fitted scaling relations in Figs. S3 (c - f) are given by $S_1(r) = (0.420 \pm 0.011) [S_3(r)]^{0.439 \pm 0.011}$, $S_2(r) = (0.457 \pm 0.021) [S_3(r)]^{0.820 \pm 0.022}$, $S_4(r) = (3.316 \pm 0.220) [S_3(r)]^{1.069 \pm 0.033}$, and $S_5(r) = (13.794 \pm 1.061) [S_3(r)]^{1.118 \pm 0.038}$, obtained from the orthogonal distance regression, with the uncertainties in $S_p(r)$ given by their corresponding standard deviations. This broader scaling range allows for a more reliable determination of the Kolmogorov exponents, as shown in Fig. S3 (b). We observe deviations from the K41 prediction, $\zeta(p) = p/3$, consistent with results reported in both classical and quantum turbulence [18, 62, 65]. Such deviations can be accounted for by a refinement of the K41 prediction. In particular, we test the K62 formulation, which introduces intermittency corrections and predicts $\zeta(p) = p/3 - \kappa p(p-3)/2$, where κ is a constant [66]. As shown in Fig. S3 (b), the measured exponents are in good agreement with the K62 prediction, with fitting parameter $\kappa = 0.114 \pm 0.006$.

UNIVERSALITY OF THE INCOMPRESSIBLE KINETIC ENERGY

In the main text, we argued that the incompressible kinetic energy at equilibration $E_i := (m/2) \int |\mathbf{u}_i(\mathbf{r}, t_{eq})|^2 d^2\mathbf{r} = \int_0^\infty E_i(k) dk$, scales with the quench duration as

$$E_i \propto \tau_Q^{-(1+2\nu)/(1+z\nu)}. \quad (\text{S9})$$

This follows from the observation that E_i can be approximated by a sum over the n_v vortex contributions, $E_i \simeq (m/2) n_v \int_{\mathcal{D}_\xi} |\mathbf{u}_v(\mathbf{r})|^2 d^2\mathbf{r}$, where the integration domain \mathcal{D}_ξ is set by the KZ length ξ , and the weighted velocity field of a single vortex is $\mathbf{u}_v(\mathbf{r}) = \sqrt{\rho(\mathbf{r})} \hbar/(mr) \mathbf{e}_\varphi$ with \mathbf{e}_φ being the unit vector along the azimuthal angle. We evaluate the single-vortex integral by assuming a vanishing condensate density within the core of radius r_v , and a uniform background value $\rho = \mu/g$ outside. This yields

$$\int_{\mathcal{D}_\xi} |\mathbf{u}_v(\mathbf{r})|^2 d^2\mathbf{r} \simeq \rho \frac{2\pi\hbar^2}{m^2} \int_{r_v}^{\hat{\xi}} \frac{1}{r} dr = \rho \frac{2\pi\hbar^2}{m^2} \ln\left(\frac{\hat{\xi}}{r_v}\right). \quad (\text{S10})$$

The factor $\ln(\hat{\xi}/r_v)$ grows only logarithmically with $\hat{\xi}$, making it a sub-leading correction to the power-law (S9), which is governed by the scaling of n_v and ρ at equilibration time, as discussed in the main text. We tested the prediction in Eq. (S9) numerically for two different temperature values in Fig. S4, and the results support this scaling within numerical uncertainty. The fitted power laws in Fig. S4 are $E_i = (19.774 \pm 5.010) \times 10^4 \tau_Q^{-0.971 \pm 0.052}$ for panel (a) and $E_i = (9.543 \pm 2.951) \times 10^4 \tau_Q^{-0.935 \pm 0.068}$ in panel (b), confirming the predicted τ_Q^{-1} behavior based on the mean-field values of the critical exponents $\nu = 1/2$ and $z = 2$. For all fits with exact independent variables, we use weighted least squares with weights given by the inverse variances.

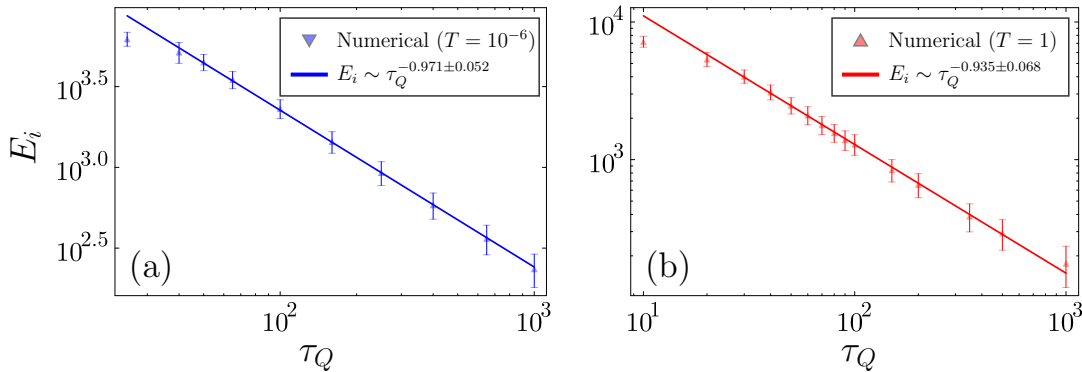


Figure S4. **Kibble-Zurek universality of the incompressible kinetic energy.** Panels (a) and (b) show the incompressible kinetic energy E_i at the equilibration time for various quench times τ_Q at temperature $T = 10^{-6}$ and $T = 1$, respectively. Each data point is averaged over (a) $\mathcal{R} = 2000$ and (b) $\mathcal{R} = 1000$ stochastic realizations. In both panels, error bars denote one standard deviation.

UNIVERSALITY OF THE COMPRESSIBLE KINETIC ENERGY AND ITS SPECTRUM

Having established the universal scaling of the incompressible kinetic energy and its spectrum, we now turn to analyze the compressible component across different quench durations τ_Q . Fig. S5 shows the corresponding spectra $E_c(k)$, which exhibit a substantial collapse onto a single curve, indicating an approximate independence from τ_Q . This is also reflected in the total compressible energy E_c , shown in Fig. S6 (b), where a power-law fit yields $E_c = (3.977 \pm 0.120) \times 10^3 \tau_Q^{-0.019 \pm 0.006}$. The reason for this behavior is that, at the simulation temperature $T = 1$ (corresponding to a physical temperature of $O(1)$ nK for parameters relevant to homogeneous quasi-2D BEC experiments [32] and used throughout the main text), condensate-density modulations contributing to E_c are predominantly due to thermal fluctuations, and are therefore independent of τ_Q . This interpretation is supported by additional simulations at $T = 10^{-6}$ ($O(10^{-6})$ nK), where the magnitude of E_c decreases by nearly two orders of magnitude compared to the $T = 1$ case (see Fig. S6 (a,b)).

At $T = 10^{-6}$, the suppression of thermal fluctuations allows density modulations arising from phonons emitted during vortex–antivortex annihilation to contribute more noticeably to the compressible energy. The corresponding spectra for different τ_Q are shown in Fig. S6 (c), and, unlike the $T = 1$ case, they are clearly distinct. This naturally raises the question of whether a rescaling in τ_Q can restore their collapse. To address this, we assume that E_c originates purely from vortex–antivortex annihilations. The total number of emitted phonons at equilibration, N_p , is proportional to the number of annihilation events and therefore to the total number of vortices n_v in a periodic system, where vortices and antivortices appear in equal numbers. According to the Kibble–Zurek mechanism (KZM), this implies $N_p \propto n_v \propto \hat{\xi}^{-2} \propto \tau_Q^{-2\nu/(1+z\nu)}$ in two spatial dimensions, where $\hat{\xi}$ is the Kibble–Zurek correlation length and ν and z are the correlation-length and dynamic critical exponents, respectively. Let $n_p(k)$ denote the phonon number density at momentum $\hbar k$, defined such that $\int_0^\infty n_p(k) dk = N_p$. At equilibration, $\hat{\xi}$ sets the characteristic momentum scale of the spectrum, motivating the scaling ansatz $n_p(k) = \tau_Q^{-\alpha} F_p(k\hat{\xi})$, where $F_p(x)$ is a function of the scaling variable $x = k\hat{\xi}$. Integrating over all momenta gives

$$\int_0^\infty n_p(k) dk \propto \tau_Q^{-\alpha} \hat{\xi}^{-1} \propto \tau_Q^{-\alpha-\nu/(1+z\nu)}, \quad (\text{S11})$$

which fixes $\alpha = \nu/(1+z\nu)$. Each phonon carries energy $\hbar k c_s$, where $c_s = \sqrt{\mu/m}$ is the speed of sound in the condensate [14]. For a linear quench of the chemical potential $\mu(t)$, we have $\mu(t_{eq}) \propto \tau_Q^{-1/(1+z\nu)}$, giving the total phonon energy

$$E_p^{\text{tot}} = \int_0^\infty n_p(k) \hbar k c_s dk \propto \tau_Q^{-\alpha} \tau_Q^{-2\nu/(1+z\nu)} \sqrt{\mu(t_{eq})} \propto \tau_Q^{-(3\nu+1/2)/(1+z\nu)}. \quad (\text{S12})$$

The corresponding spectral density is

$$E_p^{\text{tot}}(k) \propto \tau_Q^{-(2\nu+1/2)/(1+z\nu)} G\left(k\tau_Q^{\nu/(1+z\nu)}\right), \quad (\text{S13})$$

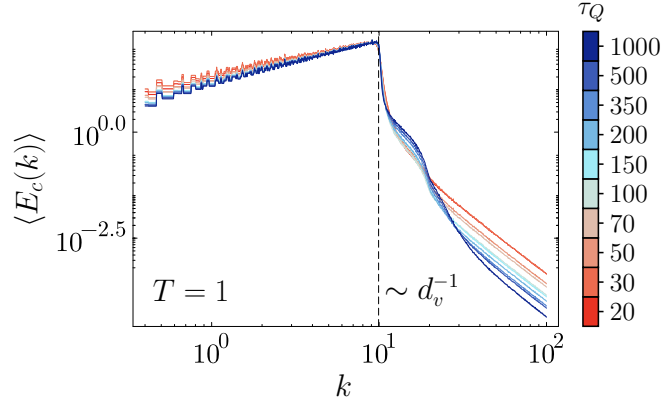


Figure S5. **Compressible kinetic energy spectra at temperature $T = 1$.** Ensemble-averaged compressible kinetic energy spectra $\langle E_c(k) \rangle$ at equilibration time for various quench durations τ_Q at $T = 1$. Each curve is obtained by averaging over $\mathcal{R} = 1000$ stochastic realizations. The dashed vertical line indicates $k = 2\pi/d_v$, where $d_v = 4\xi_h$ estimates the vortex diameter, with ξ_h the healing length. Shaded regions denote 95% confidence intervals.

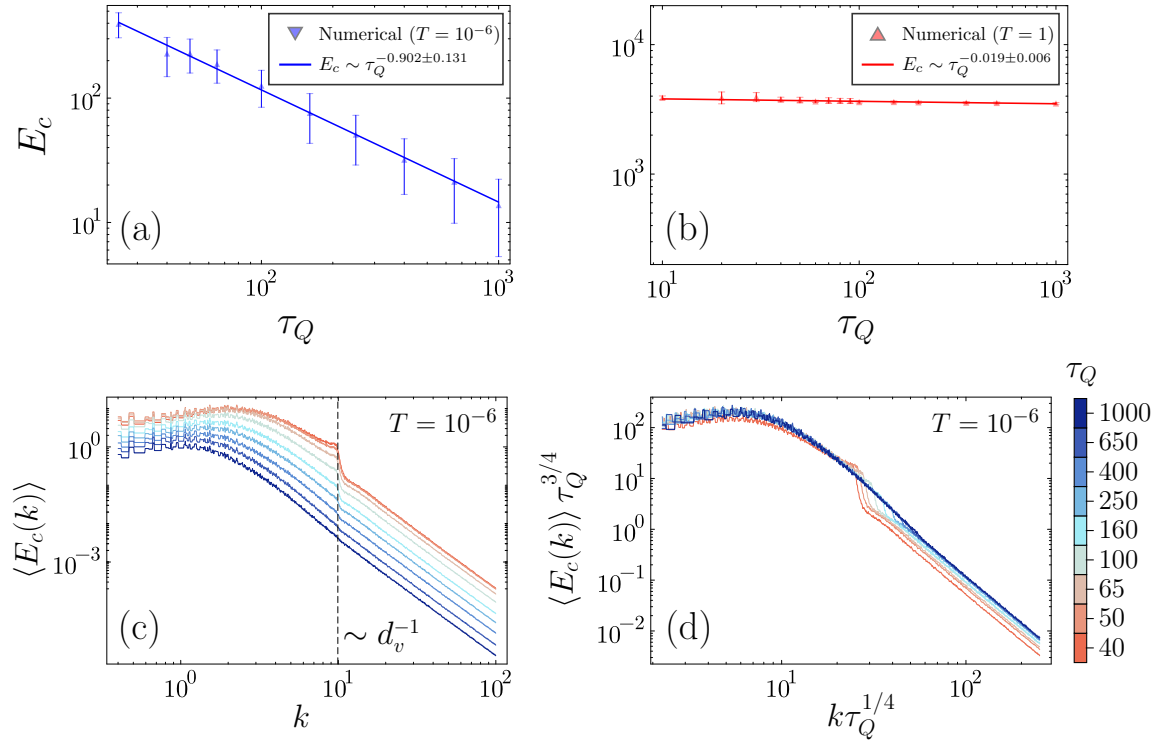


Figure S6. **Kibble-Zurek universality of the compressible kinetic energy.** Panels (a) and (b) show the compressible kinetic energy E_c at equilibration for various quench durations τ_Q at temperatures $T = 10^{-6}$ and $T = 1$, respectively. Each curve in (a) and (b) is obtained by averaging over $\mathcal{R} = 2000$ and $\mathcal{R} = 1000$ stochastic realizations, respectively. Error bars denote one standard deviation. Panel (c) shows the ensemble-averaged spectrum $\langle E_c(k) \rangle$ at equilibration for several values of τ_Q at $T = 10^{-6}$, each curve averaged over $\mathcal{R} = 2000$ realizations. The dashed vertical line indicates $k = 2\pi/d_v$, where $d_v = 4\xi_h$ estimates the vortex diameter, with ξ_h the healing length. Panel (d) displays $\langle E_c(k) \rangle \tau_Q^{3/4}$ as a function of the scaled momentum $k\tau_Q^{1/4} \propto k\xi_h$. In panels (c) and (d), shaded error bands denote 95% confidence intervals.

where G denotes the general function encoding the spectral shape. For the mean-field exponents $\nu = 1/2$ and $z = 2$, Eq. (S12) gives $E_p^{\text{tot}} \propto \tau_Q^{-1}$. Hence, if E_c is primarily due to vortex-antivortex annihilation, one expects $E_c \propto \tau_Q^{-1}$. This prediction is tested in Fig. S6 (a), where the fitted power law is $E_c = (7.422 \pm 4.679) \times 10^3 \tau_Q^{-0.902 \pm 0.131}$. Furthermore, Eq. (S13) implies that $E_c(k)\tau_Q^{3/4}$ should collapse when plotted against $k\tau_Q^{1/4}$. Such a collapse is indeed observed in Fig. S6 (d). As a final remark, we note that although the rescaling in τ_Q required to obtain an overlap of the spectra is the same in the mean-field regime for both the compressible and incompressible energy spectra, this is purely a coincidence due to the mean-field values of the critical exponents. In fact, the corresponding general scaling forms differ (compare Eq. (S13) with Eq. (4) of the main text).

TIME EVOLUTION OF THE INCOMPRESSIBLE KINETIC ENERGY SPECTRUM, ENSTROPY, AND VORTEX NUMBER

Throughout this work, we have focused on the study of spontaneous quantum turbulence at equilibration time, when the predictions of the Kibble-Zurek (KZ) mechanism are valid. It is however also interesting to consider the full time evolution of the system to observe how the turbulent dynamics unfold. Specifically, in Fig. S7, we show the time evolution of the incompressible kinetic energy spectrum $E_i(k)$ in a single simulation run for a fast quench ($\tau_Q = 30$, upper panels) and a slower quench ($\tau_Q = 350$, lower panels). Near the equilibration time, the $k^{-5/3}$ Kolmogorov scaling emerges, signaling the onset of spontaneous quantum turbulence in the newborn condensate. This scaling regime remains visible during the subsequent evolution until all vortices are annihilated, as indicated by a sudden decay in the amplitude of $E_i(k)$. The extent of the inertial range, where the $k^{-5/3}$ power law is observed, is relatively

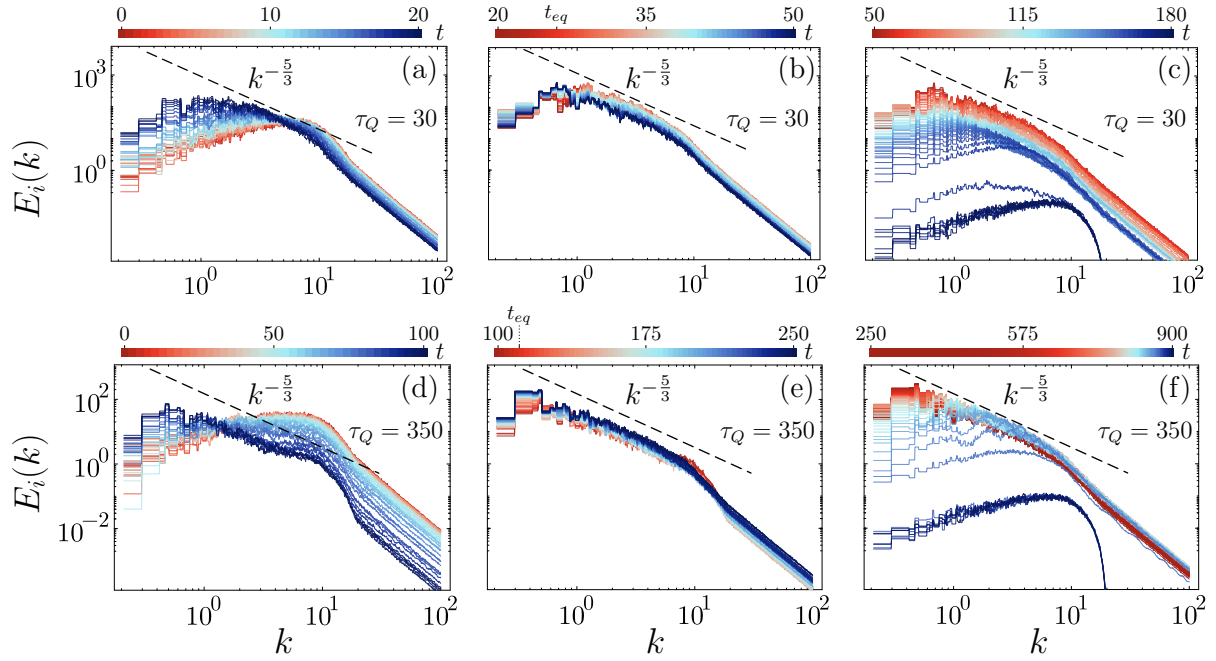


Figure S7. **Time evolution of the incompressible kinetic energy spectrum.** Panels (a), (b) and (c) show subsequent intervals of time evolution of the incompressible kinetic energy spectrum $E_i(k)$ in a single trajectory of the system for a quench of duration $\tau_Q = 30$. The equilibration time in this case is $t_{eq} = 25.9$. Panels (d), (e) and (f) show the same for $\tau_Q = 350$, where $t_{eq} = 111.5$. In both cases the quench starts at $t = 0$.

narrow for the fast quench ($\tau_Q = 30$, see Fig. S7(b)), whereas for the slower quench ($\tau_Q = 350$, see Fig. S7(e)) it becomes broader, spanning nearly a decade in k . This behavior is consistent with the range being bounded by the dissipation scale, set by the vortex-core size, and the injection scale, given by the inter-vortex distance determined by the KZ length ξ : as ξ decreases for faster quenches, the inertial-range window naturally shrinks.

Besides the energy spectrum, we have also examined the time evolution of the enstrophy, defined as

$$\Omega_u(t) = \int |\nabla \times \mathbf{u}(\mathbf{r}, t)|^2 d^2 \mathbf{r}, \quad (\text{S14})$$

where $\nabla \times \mathbf{u}$ denotes the vorticity associated with the weighted superfluid velocity field. In two-dimensional (2D) classical turbulence, the conservation of enstrophy plays a key role, as it leads to an inverse energy cascade characterized by the formation of increasingly larger eddies. In quantum turbulence (QT), a similar mechanism can occur through the clustering of same-sign vortices, resulting in extended regions of high vorticity. However, in 2D QT, enstrophy is not necessarily conserved, and this can give rise to a direct energy cascade [16–18]. Fig. S8 shows the time

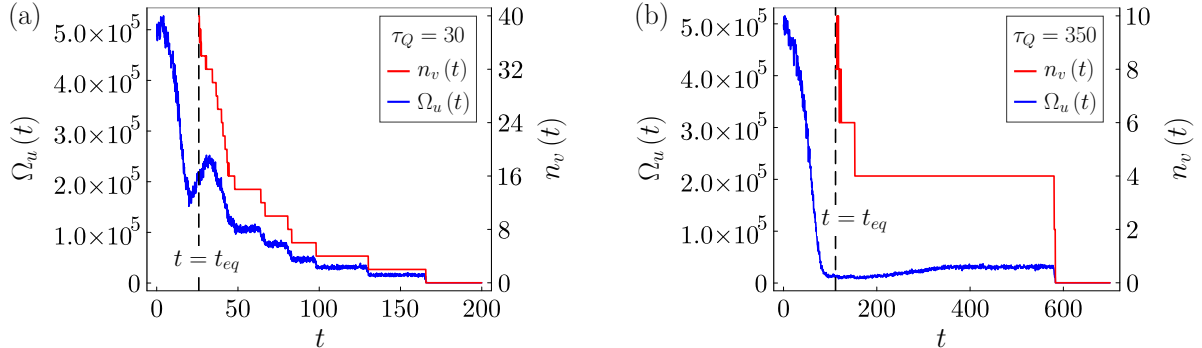


Figure S8. **Number of vortices $n_v(t)$ and enstrophy $\Omega_u(t) = \int |\nabla \times \mathbf{u}(\mathbf{r}, t)|^2 d^2 \mathbf{r}$ as functions of time t .** The data are from the same $T = 1$ simulations as in Fig. S7, with quench times (a) $\tau_Q = 30$ ($t_{eq} = 25.9$) and (b) $\tau_Q = 350$ ($t_{eq} = 111.5$).

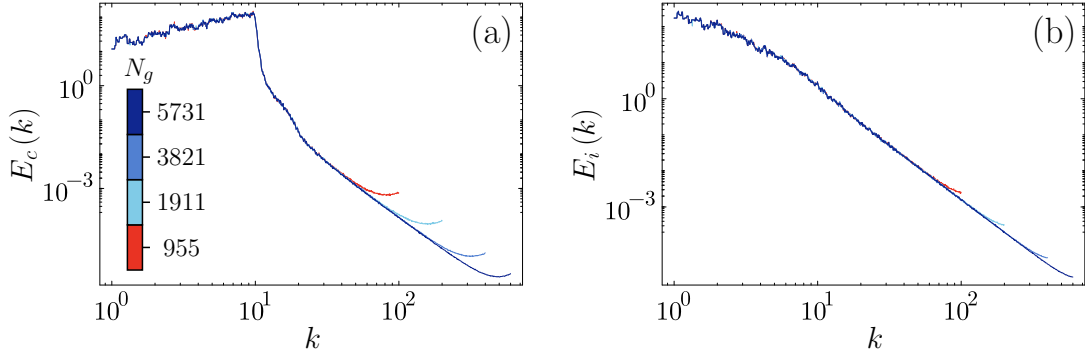


Figure S9. **Kinetic energy spectrum calculated using the quadrature method.** (a) Compressible kinetic energy spectrum $E_c(k)$ as a function of k for different grid sizes N_g . (b) Incompressible kinetic energy spectrum $E_i(k)$ as a function of k for the same N_g . Both panels correspond to a quench time of $\tau_Q = 60$, evaluated at the equilibration time. For this analysis, a single realization was selected from the 1000 independent noise realizations to determine the optimal N_g . Each N_g is chosen according to $N_g = 2\lfloor Lk_m/2\pi \rfloor + 1$, with $k_m = 100, 200, 400$, and 600 .

evolution of the enstrophy together with the vortex count from the same data used in Fig. S7, for $\tau_Q = 30$ in panel (a) and $\tau_Q = 350$ in (b). The results indicate that enstrophy is not conserved throughout the evolution, suggesting the presence of a direct energy cascade. Moreover, tracking the vortex positions over time reveals no formation of same-sign vortex clusters.

NUMERICAL EVALUATION OF THE COMPRESSIBLE AND INCOMPRESSIBLE ENERGY SPECTRA

Given the weighted superfluid velocity \mathbf{u} , we outline the procedure to extract its irrotational and solenoidal components, \mathbf{u}_c and \mathbf{u}_i , respectively.

Using the Green's function [76], any two-dimensional vector field $\mathbf{V}(\mathbf{r})$ can be expressed as

$$\mathbf{V}(\mathbf{r}) = \int \mathbf{V}(\mathbf{r}') \delta(\mathbf{r} - \mathbf{r}') d^2\mathbf{r}' = \nabla^2 \left[\frac{1}{2\pi} \int \mathbf{V}(\mathbf{r}') \ln\left(\frac{|\mathbf{r} - \mathbf{r}'|}{l}\right) d^2\mathbf{r}' \right], \quad (\text{S15})$$

where $\delta(\mathbf{r})$ is the two-dimensional Dirac delta function and l is a constant with units of length. Applying Eq. (S15) to $\mathbf{u}(\mathbf{r})$ yields $\mathbf{u}(\mathbf{r}) = \nabla^2 \mathbf{b}(\mathbf{r})$, where $\mathbf{b}(\mathbf{r}) := (1/2\pi) \int \mathbf{u}(\mathbf{r}') \ln(|\mathbf{r} - \mathbf{r}'|/l) d^2\mathbf{r}'$. Using the vector identity $\nabla \times (\nabla \times \mathbf{A}) = \nabla(\nabla \cdot \mathbf{A}) - \nabla^2 \mathbf{A}$, we can thus decompose \mathbf{u} into:

$$\mathbf{u}_c(\mathbf{r}, t) = \nabla[\nabla \cdot \mathbf{b}(\mathbf{r}, t)], \quad \mathbf{u}_i(\mathbf{r}, t) = -\nabla \times [\nabla \times \mathbf{b}(\mathbf{r}, t)], \quad (\text{S16})$$

satisfying $\nabla \times \mathbf{u}_c(\mathbf{r}, t) = 0$ and $\nabla \cdot \mathbf{u}_i(\mathbf{r}, t) = 0$.

In Fourier space, we have $\tilde{\mathbf{u}}(\mathbf{k}) = -k^2 \tilde{\mathbf{b}}(\mathbf{k})$, with $\tilde{\mathbf{b}}(\mathbf{k}, t) = (1/2\pi) \int e^{-i\mathbf{k} \cdot \mathbf{r}} \mathbf{b}(\mathbf{r}, t) d^2\mathbf{r}$. Inserting this into Eq. (S16) gives:

$$\mathbf{u}_c(\mathbf{r}, t) = \frac{1}{2\pi} \int \frac{\mathbf{k}}{k^2} [\mathbf{k} \cdot \tilde{\mathbf{u}}(\mathbf{k}, t)] e^{i\mathbf{k} \cdot \mathbf{r}} d^2\mathbf{k}, \quad \mathbf{u}_i(\mathbf{r}, t) = -\frac{1}{2\pi} \int \frac{\mathbf{k}}{k^2} \times [\mathbf{k} \times \tilde{\mathbf{u}}(\mathbf{k}, t)] e^{i\mathbf{k} \cdot \mathbf{r}} d^2\mathbf{k}, \quad (\text{S17})$$

where $k := |\mathbf{k}|$. Thus, in momentum space, the compressible and incompressible components of \mathbf{u} read $\tilde{\mathbf{u}}_c(\mathbf{k}, t) = \mathbf{e}_k [\mathbf{e}_k \cdot \tilde{\mathbf{u}}(\mathbf{k}, t)]$, and $\tilde{\mathbf{u}}_i(\mathbf{k}, t) = \tilde{\mathbf{u}}(\mathbf{k}, t) - \tilde{\mathbf{u}}_c(\mathbf{k}, t)$ where $\mathbf{e}_k := \mathbf{k}/k$. Finally, the compressible and incompressible energy spectra are given by

$$E_c(k, t) = \frac{m}{2} k \int_0^{2\pi} [\mathbf{e}_k \cdot \tilde{\mathbf{u}}^*(\mathbf{k}, t)] [\mathbf{e}_k \cdot \tilde{\mathbf{u}}(\mathbf{k}, t)] d\varphi_k, \quad E_i(k, t) = \frac{m}{2} k \int_0^{2\pi} \tilde{\mathbf{u}}^*(\mathbf{k}, t) \cdot \tilde{\mathbf{u}}(\mathbf{k}, t) d\varphi_k - E_c(k), \quad (\text{S18})$$

where φ_k is the azimuthal angle of \mathbf{k} , i.e., $\mathbf{e}_k = (\cos \varphi_k, \sin \varphi_k)$. As our analysis mainly focuses on the system at equilibration time t_{eq} , we will omit the time argument for brevity and denote $E_{c,i}(k) := E_{c,i}(k, t_{eq})$.

To numerically evaluate $E_{c,i}(k)$ as given in Eqs. (S18), we used the Julia package FFTW.jl, which provides an interface to the FFTW3 library [77], allowing efficient computation of the fast Fourier transform to obtain $\tilde{\mathbf{u}}(\mathbf{k})$. To

perform the angular integral over φ_k , we employed the quadrature method introduced in [44]. Denoting by k_m the maximum wavenumber considered for evaluating $E_{c,i}(k)$, and by N_g the number of grid points along each spatial direction for a periodic system of size $L \times L$, we compute and plot $E_c(k)$ and $E_i(k)$ for different values of N_g in Fig. S9. It clearly shows that sufficiently large values of N_g are required to suppress numerical errors at high wavenumbers k . We found that the minimal grid size needed to ensure accuracy for $k \leq k_m$ is approximately $N_g \approx 8\lfloor Lk_m/2\pi \rfloor + 1$, where $\lfloor x \rfloor$ denotes the nearest integer to x . Accordingly, we used $N_g = 3817$ to accurately compute $E_{c,i}(k)$ up to $k \leq 100$.

NUMERICAL EVALUATION OF THE VELOCITY STRUCTURE FUNCTION

To numerically calculate the velocity structure function

$$S_p(r) := \frac{1}{2\pi L^2} \int_0^{2\pi} \int_0^L \int_0^L |[\mathbf{u}_i(\mathbf{R} + \mathbf{r}) - \mathbf{u}_i(\mathbf{R})] \cdot \mathbf{e}_r|^p \, dR_x \, dR_y \, d\varphi, \quad (\text{S19})$$

where $\mathbf{e}_r := \mathbf{r}/r = (\cos \varphi, \sin \varphi)$ is the unit vector along \mathbf{r} [2, 64], we compute the velocity increments using the discrete Fourier transform, implemented via the Julia package FFTW.jl. Let $\nu_j := (j-1)L_\nu/N_\nu$ for $1 \leq j \leq N_\nu$ with $\nu = x, y$. The weighted superfluid velocity $\mathbf{u}(x_j, y_l)$ can then be written as

$$\mathbf{u}(x_j, y_l) = \frac{1}{N_x N_y} \sum_{n_x=1}^{N_x} \sum_{n_y=1}^{N_y} \mathbf{C}(n_x, n_y) e^{2\pi i (n_x-1)(j-1)/N_x} e^{2\pi i (n_y-1)(l-1)/N_y}, \quad (\text{S20})$$

where $\mathbf{C}(n_x, n_y)$ are the Fourier coefficients. Since $\mathbf{u}(x_j, y_l)$ is real, its derivatives must also be real. Using the identity $\exp(2\pi i (n_\nu - 1)(j-1)/N_\nu) = \exp(2\pi i (n_\nu - 1 - N_\nu)(j-1)/N_\nu)$ for any integers $1 \leq n_\nu \leq N_\nu$ and $1 \leq j \leq N_\nu$, in order to make $\mathbf{u}_i(x_j, y_l)$ real, one should use the following expression:

$$\mathbf{u}_i(x_j, y_l) = \frac{1}{N_x N_y} \sum_{n_x=1}^{N_x} \sum_{n_y=1}^{N_y} \left\{ \mathbf{C}(n_x, n_y) - [\mathbf{k}(n_x, n_y) \cdot \mathbf{C}(n_x, n_y)] \frac{\mathbf{k}(n_x, n_y)}{k^2(n_x, n_y)} \right\} e^{2\pi i (n_x-1)(j-1)/N_x} e^{2\pi i (n_y-1)(l-1)/N_y}, \quad (\text{S21})$$

with $\mathbf{k}(n_x, n_y) := \sum_{\nu=x,y} k_\nu(n_x, n_y) \mathbf{e}_\nu$ and

$$k_\nu(n_x, n_y) := \begin{cases} 2\pi i (n_\nu - 1)/L_\nu, & \text{if } 1 \leq n_\nu \leq [N_\nu/2]_r + 1, \\ 2\pi i (n_\nu - 1 - N_\nu)/L_\nu, & \text{otherwise,} \end{cases} \quad (\text{S22})$$

where $[x]_r$ is the greatest integer less than or equal to x , so that $-2\pi i [N_\nu/2]_r / L_\nu \leq k_\nu(n_x, n_y) \leq 2\pi i [N_\nu/2]_r / L_\nu$.